Earth and Planetary Science Letters 598 (2022) 117842

Contents lists available at ScienceDirect

Earth and Planetary Science Letters

www.elsevier.com/locate/epsl

Early Jurassic massive release of terrestrial mercury linked to floral crisis

Xin Jin [a,b], Fei Zhang [b,*], Viktória Baranyi [c], David B. Kemp [d,e], Xinbin Feng [f], Stephen E. Grasby [g], Guangyi Sun [f], Zhiqiang Shi [a], Wenhan Chen [d,e], Jacopo Dal Corso [d,*]

[a] State Key Laboratory of Oil and Gas Reservoir Geology and Exploitation and Key Laboratory of Deep-Time Geography and Environment Reconstruction and Applications of Ministry of Natural Resources, Chengdu University of Technology, Chengdu 610059, China
[b] State Key Laboratory of Loess and Quaternary Geology, Institute of Earth Environment, Chinese Academy of Sciences, Xi'an 710061, China
[c] Department of Geology, Croatian Geological Survey, Sachsova 2, P.O. Box 268, HR-10000 Zagreb, Croatia
[d] State Key Laboratory of Biogeology and Environmental Geology, China University of Geosciences, Wuhan 430074, China
[e] Hubei Key Laboratory of Critical Zone Evolution, School of Earth Sciences, China University of Geosciences, Wuhan 430074, China
[f] State Key Laboratory of Environmental Geochemistry, Institute of Geochemistry, Chinese Academy of Sciences, Guiyang 550081, China
[g] Geological Survey of Canada, Natural Resources Canada, 3303 33rd Street N.W., Calgary, Alberta T2L 2A7, Canada

ARTICLE INFO

Article history:
Received 11 June 2022
Received in revised form 13 August 2022
Accepted 24 September 2022
Available online 6 October 2022
Editor: B. Wing

Keywords:
Jurassic
Toarcian Oceanic Anoxic Event
mercury
vegetation crisis

ABSTRACT

The Toarcian Oceanic Anoxic Event (T-OAE, ~183 Ma) was marked by a pronounced negative carbon-isotope excursion, rapid global warming, ocean deoxygenation, and turnover of marine and terrestrial biota. The T-OAE has been linked to carbon (C) release from volcanism, but the mechanisms controlling the cycling of C, metals, and nutrients during the event are still not fully understood. Here we show that lacustrine strata (Anya section) through the T-OAE in the Ordos Basin (China) record large increases in Hg/TOC (up to 453 ppb/wt.% relative to a background of 23 ppb/wt.%), which are coincident with the sudden demise of spore producing plants and seed ferns and the acme of *Classopollis* pollen of the thermophilic Cheirolepidiaceae conifers. These changes occurred during the peak of the negative carbon-isotope excursion that marks the T-OAE in the Anya section. Hg-isotopes are a useful proxy for recognizing changes in Hg sources and fluxes (notably from atmospheric deposition and terrestrial biomass) in sediments and sedimentary rocks. The negative Δ^{199}Hg and δ^{202}Hg throughout the Anya section are consistent with a constant terrestrial Hg source in the studied interval. Hence, the recorded Hg enrichment suggests that terrestrial Hg loading increased during the T-OAE. Coupled with evidence for a large increase in hydrological cycling, weathering and runoff, our data indicate that the T-OAE floral crisis was associated with a massive release of terrestrial Hg to oceanic and terrestrial ecosystems. This work provides new insights into the links between toxic metal cycling and mass extinction during times of large-scale volcanism.

1. Introduction

The Toarcian Oceanic Anoxic Event (T-OAE; ~183 Ma; Early Jurassic) (Jenkyns, 1988), was coincident with a 6–10 °C warming of seawater (e.g., Bailey et al., 2003; Suan et al., 2008), widespread ocean deoxygenation (e.g., Kemp et al., 2022), an accelerated hydrological cycle (e.g., Dera et al., 2009), and a rapid increase in atmospheric pCO_2 (up to 1200 ± 400 ppmv) (McElwain et al., 2005; Ruebsam et al., 2020). These large-scale environmental changes led to a biotic crisis of many groups on land and in the sea (e.g., Little and Benton, 1995; Caruthers et al., 2014; Slater et al., 2019). The event is marked by a globally synchronous negative carbon-isotope excursion (NCIE) that has been attributed to the injection of isotopically light carbon into the exogenic C-cycle. However, the source of this carbon is debated, and has been linked to effusion from large scale volcanic activities e.g., the Karoo-Ferrar Large Igneous Province (LIP) or the associated Chon Aike volcanic complex (McElwain et al., 2005), the dissociation of methane hydrates (Hesselbo et al., 2000; Kemp et al., 2005), and/or massive decomposition of terrestrial organic matter (Pieńkowski et al., 2016).

Sedimentary mercury (Hg) geochemistry can help constraining the potential carbon sources that triggered the T-OAE. Volcanism is the main source of Hg to the natural environment, representing up

* Corresponding authors.
E-mail addresses: zhangfei@ieecas.cn (F. Zhang), j.dalcorso@cug.edu.cn (J. Dal Corso).

https://doi.org/10.1016/j.epsl.2022.117842
0012-821X/

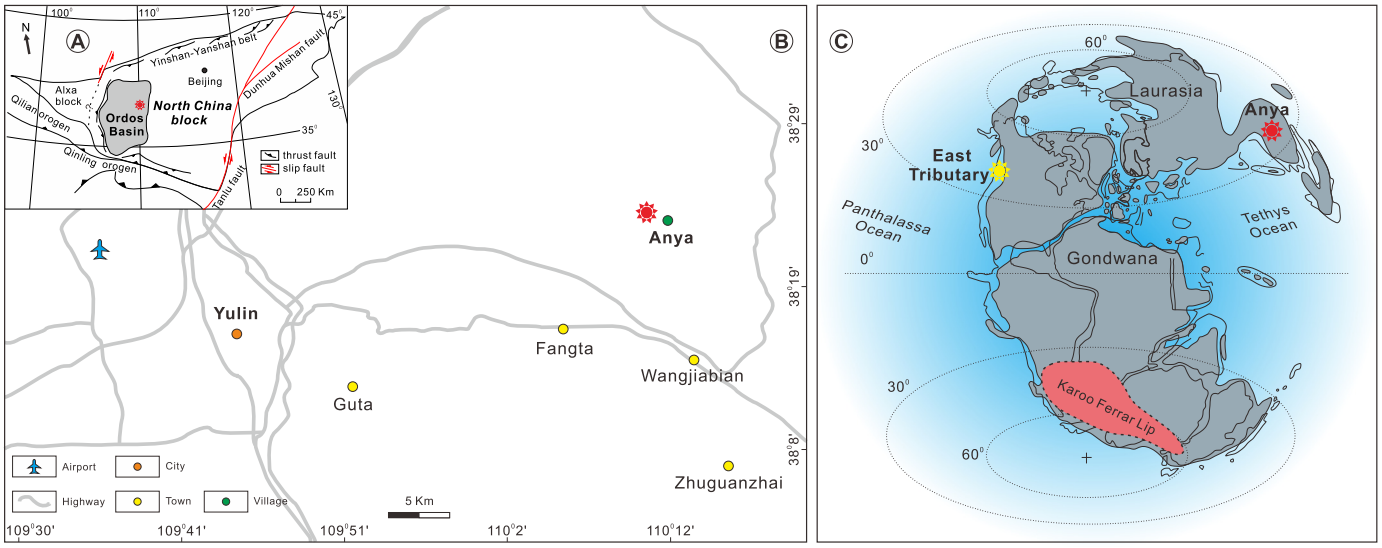

Fig. 1. Study area. A. Simplified tectonic map showing the position of Ordos Basin in the North China block (modified from Meng et al., 2019); B. Map of the Yulin area showing the location of the Anya section ca. 40 km northeast of Yulin city; C. Early Jurassic paleogeography (modified from Xu et al., 2018) showing locations of Anya section and East Tributary section (Canada) discussed in the text (Them et al., 2019). The fine dashed lines represent palaeolatitudes. The location of the Anya section is shown in red markers in the A, B, C. (For interpretation of the colors in the figure(s), the reader is referred to the web version of this article.)

to ~40% of natural emissions (Pyle and Mather, 2003). Volcanically emitted Hg has a short residence time relative to geological timescales: ca. 0.5−1 yr in the atmosphere and hundreds of years in seawater (e.g., Selin, 2009). It can be transported around the world relatively rapidly through the atmosphere before removal to Earth's surface environment. Consequently, Hg enrichments can be used as a proxy for identifying periods of enhanced volcanic activity in the geological record (Grasby et al., 2019). Mercury has seven stable isotopes with the following atomic weights and conventional percent abundances: ^{196}Hg (0.146%), ^{198}Hg (10.02%), ^{199}Hg (16.84%), ^{200}Hg (23.13%), ^{201}Hg (13.22%), ^{202}Hg (29.80%), and ^{204}Hg (6.85%) (Blum et al., 2014). These isotopes offer an opportunity for tracing the sources and pathways of Hg in the environment (Blum et al., 2014). This is because mass-dependent fractionations (MDF, reported as δ^{202}Hg) and mass-independent fractionations (odd-MIF, reported as Δ^{199}Hg and Δ^{201}Hg) have been documented in natural samples (Blum et al., 2014). Hg-MDF can result from numerous biological, abiotic chemical and physical processes (Blum et al., 2014; Grasby et al., 2017). In contrast, Hg-MIF can be useful for assessing Hg sources because only a few processes can cause Hg-MIF (Bergquist and Blum, 2007). Both natural samples and laboratory experiments have suggested that Hg-MIF may be caused by the magnetic isotope effect and the nuclear volume effect (Bergquist and Blum, 2007; Yin et al., 2010). These two processes tend to generate negative MIF values in continental systems and positive MIF values in marine systems, whereas Hg emitted via volcanic and potentially hydrothermal activities yields near-zero MIF values (Yin et al., 2016).

Previously reported Hg anomalies across the T-OAE are generally interpreted as evidence that the carbon released at the T-OAE was of volcanic origin from the Karoo-Ferrar LIP (Percival et al., 2015; Fantasia et al., 2018). However, recent sedimentary Hg abundance and isotopic data, from both coastal and deeper water settings, suggest that Hg enrichments could also be related to enhanced terrestrial Hg influx, even though an initial Hg input from volcanic sources cannot be excluded completely (Them et al., 2019). Nevertheless, the lack of data from terrestrial environments and the paucity of Hg-isotope data suitable for constraining Hg sources through the T-OAE means that this inference remains uncertain. Moreover, the mechanisms that may have triggered an increase of terrestrial Hg are unclear.

In this study, we present the first Hg concentration and Hg-isotope data from a lacustrine succession encompassing the T-OAE (Anya section, northeast Ordos Basin, China; Fig. 1). We integrate these data with palynofacies analysis to explore the causal links between pronounced vegetation changes during the event and Hg cycling.

2. The T-OAE in the Ordos Basin

The Ordos Basin was a large endorheic lake system located at sub-tropical latitudes on the North China block during the Early Jurassic (Fig. 1A). Our study was conducted at the Anya section (38°24′00″ N; 110°11′48″ E), in the northeastern part of the Ordos Basin, 40 km NE of Yulin City (Fig. 1B). The Anya section comprises a ~48 m succession of lacustrine strata assigned to the Fuxian Formation (Jin et al., 2020). It mainly consists in the lower part of sandstones and siltstones (0–7.7 m), in the middle part (7.7 m–17 m) dark-grey mudstones and laminated organic matter rich mudstones (LOMRM, also labeled as shales in Jin et al., 2020) with interbedded siderites, and in the upper part (17 m to the top) mainly silty mudstones, siltstones and sandstones (Fig. 2). Ge et al. (1989) reported trace fossils, plants, bivalves and ostracods in the studied section indicating that the depositional environment of the lower part of the Fuxian Formation was a lake.

Previous low resolution palynological data showed that the Anya section can be assigned to the Australasian *Classopollis torosa* Oppel Zone, supporting an early Toarcian age (Jin et al., 2020). The lowermost part of the section (ca. 0–5.8 m) may be Pliensbachian in age, as this interval lacks characteristic early Toarcian flora such as *Ischyosporites variegatus* (e.g., Xu et al., 2017). However, the Pliensbachian/early Toarcian boundary cannot be pinpointed precisely as both palynomorph assemblages include primarily long-ranging taxa. In the European epicontinental realm the Pliensbachian-Toarcian transition is characterized by a switch from fern-spore (e.g., *Deltoidospora*) and seed fern/conifer-related bisaccate pollen (*Alisporites* spp.) dominated palynological assemblages, to that of *Classopollis* (e.g., Slater et al., 2019). The change to a *Classopollis* assemblage is first documented at 5.8 m in the Anya section suggesting an early Toarcian age above this level (Jin et al., 2020). A negative carbon isotope excursion (NCIE) in the section is interpreted as the globally observed T-OAE NCIE (Fig. 2;

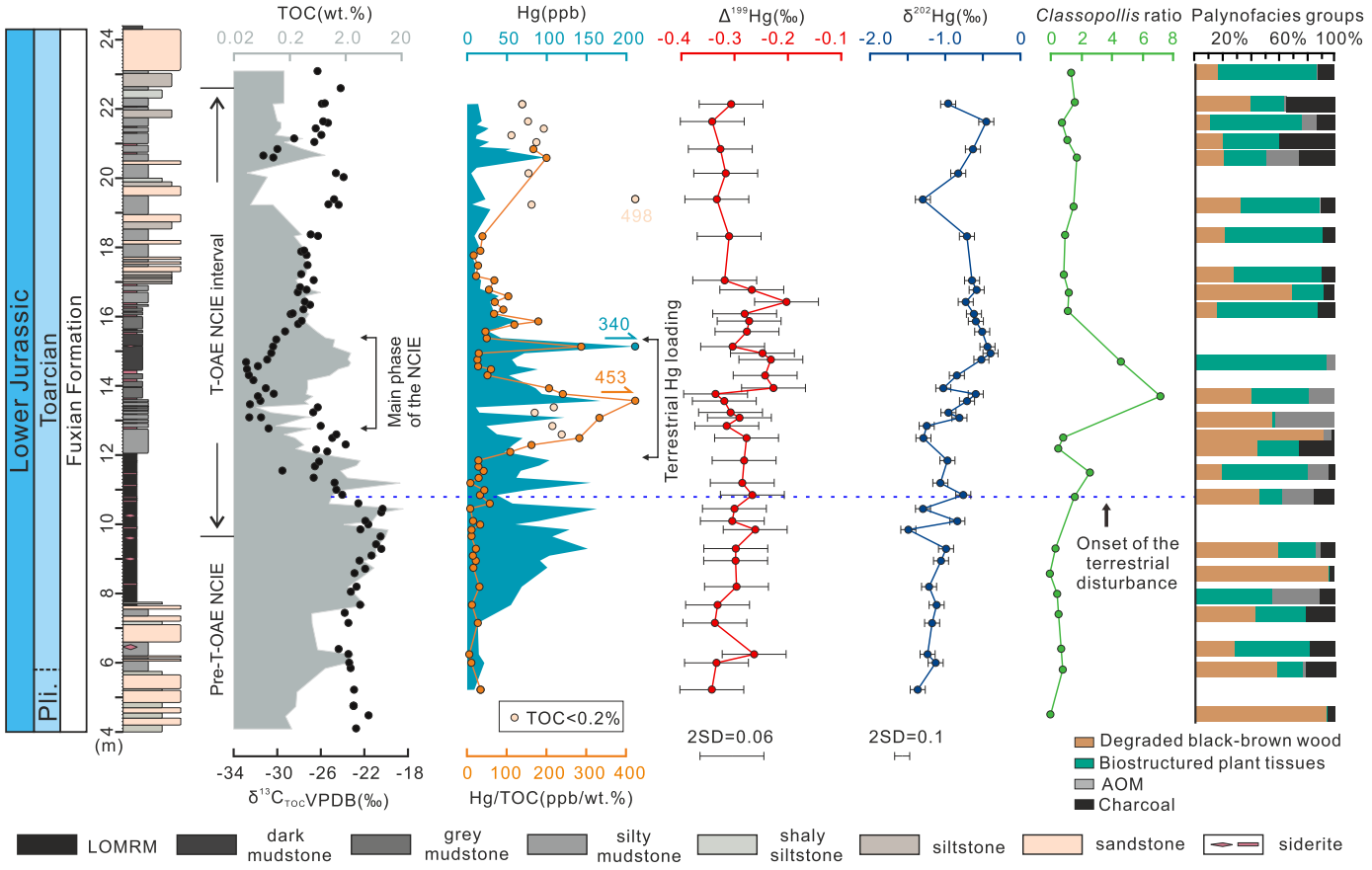

Fig. 2. Lithological column and proxy data across studied Anya section. *Classopollis* ratio (*Classopollis* counts/the sum of all other palynomorph absolute abundances), and the abundance of selected palynofacies groups are expressed as percentage proportions (%). The lithological column is refined from Jin et al. (2020). The $\delta^{13}C_{TOC}$ and TOC values are from Jin et al. (2020) and also include 15 new datapoints (this study). Hg/TOC calculated from TOC values <0.2 wt.% are labeled (see main text). LOMRM = laminated organic matter rich mudstones. NCIE = Negative carbon isotope excursion.

Jin et al., 2020). This NCIE is recognized in bulk organic matter ($\delta^{13}C_{TOC}$), and is characterized by a ca. −12.5‰ excursion, which is also coincident with a pronounced ca. −11.3‰ negative $\delta^{13}C$ excursion in long-chain *n*-alkanes (Jin et al., 2020). The T-OAE NCIE in the Anya section spans from 9.6 to 22.6 m with the onset occurring within the LOMRM interval (Fig. 2). The main phase of the NCIE (defined by the most negative $\delta^{13}C_{TOC}$ values <−30‰) spans part of the overlying mudstone interval (12.8 m to 15.4 m) with an average total organic carbon (TOC) content of ca. 0.9 wt.% and average $\delta^{13}C_{TOC}$ value of ca. −30.7‰ (Fig. 2; also see the supplementary data of Jin et al., 2020).

3. Materials and methods

In the present study, we focus on the interval from ~4 m to ~24.4 m of the Anya section across the late Pliensbachian to early Toarcian interval (Fig. 2). We present new data here along with some previous results from Jin et al. (2020). The supplementary data (SD) makes clear the distinction between newly reported data and previously published results. A total of 26 samples were collected for palynofacies analysis, including six samples from Jin et al. (2020). The samples were processed at the School of Materials and Chemistry & Chemical Engineering, Chengdu University of Technology, and at the Department of Geology, Croatian Geological Survey. The applied laboratory procedures are identical with those presented in Jin et al. (2020). Seventy-three samples (mudstones and LOMRM) were chosen for Hg concentration analysis, and 37 samples for analyses of S concentration, major and rare earth elements, and Hg-isotopes. There's no overlap between these samples and the 26 palynological samples.

Mercury concentrations were analyzed with a Milestone Direct Mercury Analyzer (DMA80 Evo). A soil Reference Standard (GBW07423, Hg = 0.030 ppm ± 0.004) was measured to ensure the data reliability. Analytical error from these standard measurements was ±4.4 ppb. Mercury isotopes were analyzed on a Nu-Plasma II CV-MC-ICP-MS (Nu Instruments Ltd., UK), and the analytical procedure followed that of Huang et al. (2015) and Sun et al. (2016). Uncertainties reported in this study based on repeated measurements of NIST-3177 (δ^{202}Hg: −0.54 ± 0.10‰; Δ^{199}Hg: 0.01 ± 0.06‰; Δ^{200}Hg: 0.03 ± 0.07‰; Δ^{201}Hg: −0.01 ± 0.05‰; 2SD, $n = 4$). Sulfur concentrations were analyzed using a Vario Macro Cube elemental analyzer (Elementar, Hanau, Germany), and sulfanilamide standard (S = 18.62%) was run throughout the analysis. Analytical precision was <5%. Major and trace elements were analyzed using an Axios advanced wavelength dispersive X-ray fluorescence (WD-XRF; PANalytical, Ea Almelo, The Netherlands), and the analytical procedure followed Jin et al. (2022). Analytical uncertainties, as checked by parallel analysis of two international standards (GSS-8 and GSD-12), was 1–2% for all major elements. Total organic carbon (TOC) content and carbon isotope ($\delta^{13}C_{TOC}$) data are partly from Jin et al. (2020), with 15 new TOC and $\delta^{13}C_{TOC}$ values added within the interval from 9.3 m to the 22.1 m to increase the resolution. These measurements followed Jin et al. (2020). Repeated analyses of standards indicate reproducibility is better than 0.12 wt.% for TOC. Full details of sample preparation and analytical techniques are provided in the supplementary information (SI).

4. Results

4.1. Geochemistry

The Hg profile shows a similar trend to the TOC profile in the Anya section (Fig. 2). Mercury concentrations begin to increase at ca. 7.1 m, prior to the NCIE, and exhibit a distinctive increasing trend to 15.4 m. Mercury concentrations in the LOMRM interval (ca. 7.7 to 12.0 m; Fig. 2) vary from 37 ppb to 163 ppb. The highest Hg concentrations (max. = 340 ppb) are recorded in overlying mudstones (ca. 12.0 to 15.2 m), which is within the main phase of the NCIE. A minor Hg peak (98 ppb) is recorded at ca. 20.6 m (Fig. 2). Hg-isotope data show negative mass-independent fractionation values (MIF; Δ^{199}Hg; avg. = −0.29‰, $n = 37$) and negative mass-dependent fractionation values (MDF; δ^{202}Hg; avg. = −0.90‰, $n = 37$) throughout the Anya section (Fig. 2).

Organic matter (OM) is generally considered to be the main host phase for Hg in sediments, thus Hg concentrations are typically normalized to total organic carbon (TOC) content (Grasby et al., 2019). Samples from the LOMRM show a very strong positive correlation between Hg and TOC ($r = 0.86$, $p < 0.01$; Fig. 3). However, Hg and TOC show a negligible correlation in the mudstones ($r = 0.22$, $p = 0.15$; Fig. 3), where TOC values (avg. = 0.6 wt.%; $n = 46$) are much lower than in the LOMRM (avg. = 6.1 wt.%; $n = 19$) and occupy a narrow range of values, making evaluation of any linear relationship between Hg and TOC difficult (Fig. 3). A pronounced peak in Hg/TOC occurs at 13.6 m, with values increasing from background (23) to 453, coincident with the main phase of the NCIE (Fig. 2). Smaller peaks in Hg/TOC (167 and 200) occur at ∼20.6 m in the section (after excluding data with TOC content <0.2%, according to the TOC threshold of Grasby et al., 2019; Fig. 2).

Sulfides (e.g., S, Zn and Ni), iron oxides (Fe, Mn) and clay minerals (Al) can also scavenge Hg in the water column and host Hg in sediments and rocks (Grasby et al., 2019; Shen et al., 2019; Jin et al., 2022). These elements show variable correlations with Hg in the LOMRM and mudstones (Fig. 3). Notably, Hg is strongly correlated with S ($r = 0.77$, $p < 0.01$) in the LOMRM samples. Insignificant relationships in the LOMRM samples exist between Hg and Zn ($r = 0.25$, $p = 0.49$), Ni ($r = 0.09$, $p = 0.80$), Al ($r = -0.50$, $p = 0.14$), Fe ($r = -0.14$, $p = 0.70$) and Mn ($r = -0.32$, $p = 0.37$) (Fig. 3). The insignificance of these correlations may stem in part from the limited data ($n = 10$, Fig. 3). In the mudstones, weak correlations exist between Hg and Ni ($r = 0.38$, $p = 0.05$) and Fe ($r = 0.34$, $p = 0.09$). However, the correlation between Hg and S is not significant ($r = 0.24$, $p = 0.22$). As with the TOC data in this facies, S concentrations are low and occupy a very narrow range of low values (consistently <0.2%). Weak/negligible and insignificant correlations also occur between Hg and Al ($r = 0.30$, $p = 0.13$), Zn ($r = 0.27$, $p = 0.17$) and Mn ($r = 0.18$, $p = 0.36$) in the mudstones ($n = 27$) (Fig. 3). All analytical results are shown in the SD.

4.2. Characteristics of the palynofacies groups

The palynofacies and sedimentary OM composition of the Anya section is dominated by terrestrially derived kerogen, mainly black-brown degraded and non-opaque biostructured phytoclasts. Aquatic palynomorphs such as acritarchs and freshwater algae (*Botryoccous braunii*) are extremely scarce. The palynofacies terminology follows Tyson (1995). Degraded non-opaque to opaque black-brown wood particles are oxidized, thermally-altered and/or likely redeposited woody material without discernible biostructure and irregular shape and edges (Tyson, 1995; Kemp et al., 2019; Jin et al., 2020). These unstructured particles are observed in various degradation stages, including subangular particles with diffuse boundaries and completely unstructured particles. The term charcoal refers to opaque, completely black phytoclasts with tabular (equant or lath) shape and straight edges that are the product of natural pyrolysis at high temperatures (Rodrigues et al., 2021). Biostructured wood is the group of non-opaque phytoclasts with striped, banded and pitted structure consistent with origin from higher land plants. These phytoclasts usually lack autofluorescence. Translucent pale yellow-green plant tissues are membranes probably originating from leaves and include leaf cuticles as well. They have moderate yellow fluorescence. Yellow-brown particles referable as amorphous organic matter (AOM) are derived from algal biomass, or they are the product of the microbial degradation of various terrestrial plant material (Tyson, 1995; Zhang et al., 2015). These particles form irregular masses with fuzzy margins without any discernible structure or rarely with more angular edges. They have weak or no autofluorescence and a “clotted” appearance under incident blue light. The AOM often masks phytoclasts and sporomorphs visible only in fluorescence mode. The palynomorph group is subdivided into eight categories (Fig. 4): 1) *Classopollis* grains, 2) *Classopollis* agglomerates (dyads, triads, tetrads, and agglomerates with >4 grains), 3) spores, 4) spore tetrads, 5) bisaccate pollen grains, 6) other pollen grains including cycadalean-bennettitalean and Araucariaceae-, Cupressaceae-related pollen; followed by aquatic palynomorphs 7) acritarchs and 8) *Botryoccus braunii*. Despite the switch from the black shale deposition to grey mudstones no obvious differences are recorded in the preservation state of the kerogen particles throughout the section. The encountered sporomorphs have translucent yellow–brown sporoderm with a spore coloration index (SCI of Batten, 2002) of 2–5 depending on the wall-thickness variations between grains and ornamentation. At 24.4 m in the uppermost part of the section, more pigmented sporomorphs with SCI 5–7 occurred with significantly darker dark brown–black sporoderm (SCI 5–7) that might be related to changes in depositional setting or reworking.

4.3. Palynofacies assemblages

Palynofacies data are presented as percentage proportions based on counting of ≥300 particles for each sample. Five major palynofacies types are identified in the Anya section with stratigraphically constrained cluster analysis (CONISS) built in Tilia/TiliaGraph (Grimm, 1987) (Fig. 5). Palynofacies 1 (PF 1) (from 4.5 m to 7.4 m) contains various phytoclast types (>20%), charcoal particles (5–20%) and various palynomorph types (5−15%) (Fig. 6). Palynofacies 2 (PF 2) of the LOMRM sequence (between 8.0 m and 9.3 m) is dominated by degraded black–brown wood particles (30−90%), charcoal (<15%) and AOM particles (∼15%) with an AOM peak of 40% at 8.0 m (Fig. 6). Palynofacies 3 (PF 3) between 10.8 m and 14.7 m coincides with the main phase of the T-OAE NCIE and is characterized by a sharp drop in the abundance of spores, bisaccate pollen grain and other pollen types, and an increase in the amount of *Classopollis* grains (10−50%) and AOM (up to 40%) (Fig. 6). Palynofacies 4 (PF 4) (from 16.1 m to 20.6 m) shows an increased heterogeneity in phytoclast abundance together with higher charcoal relative proportions and the reappearance of a more diverse palynological assemblage with various gymnosperm pollen (5−10%, *Classopollis* excluded) and abundant spores (up to 15%) in particular. Palynofacies 5 (PF 5), from 21.1 m to the top, is characterized by higher charcoal ratios (∼20%) with an additional rise in *Classopollis*. Spores (5−15%) and spore tetrads (∼5%) in particular increase in abundance in the same interval.

A significant increase in the *Classopollis* ratio (*Classopollis* counts/total spore-pollen sum) in PF 3 starts at 10.8 m, with a nearly threefold increase in *Classopollis* relative abundance (from ∼15% to ∼40%) that occurs simultaneously with the onset of the NCIE (Figs. 2 and 5). During the NCIE, high *Classopollis* rela-

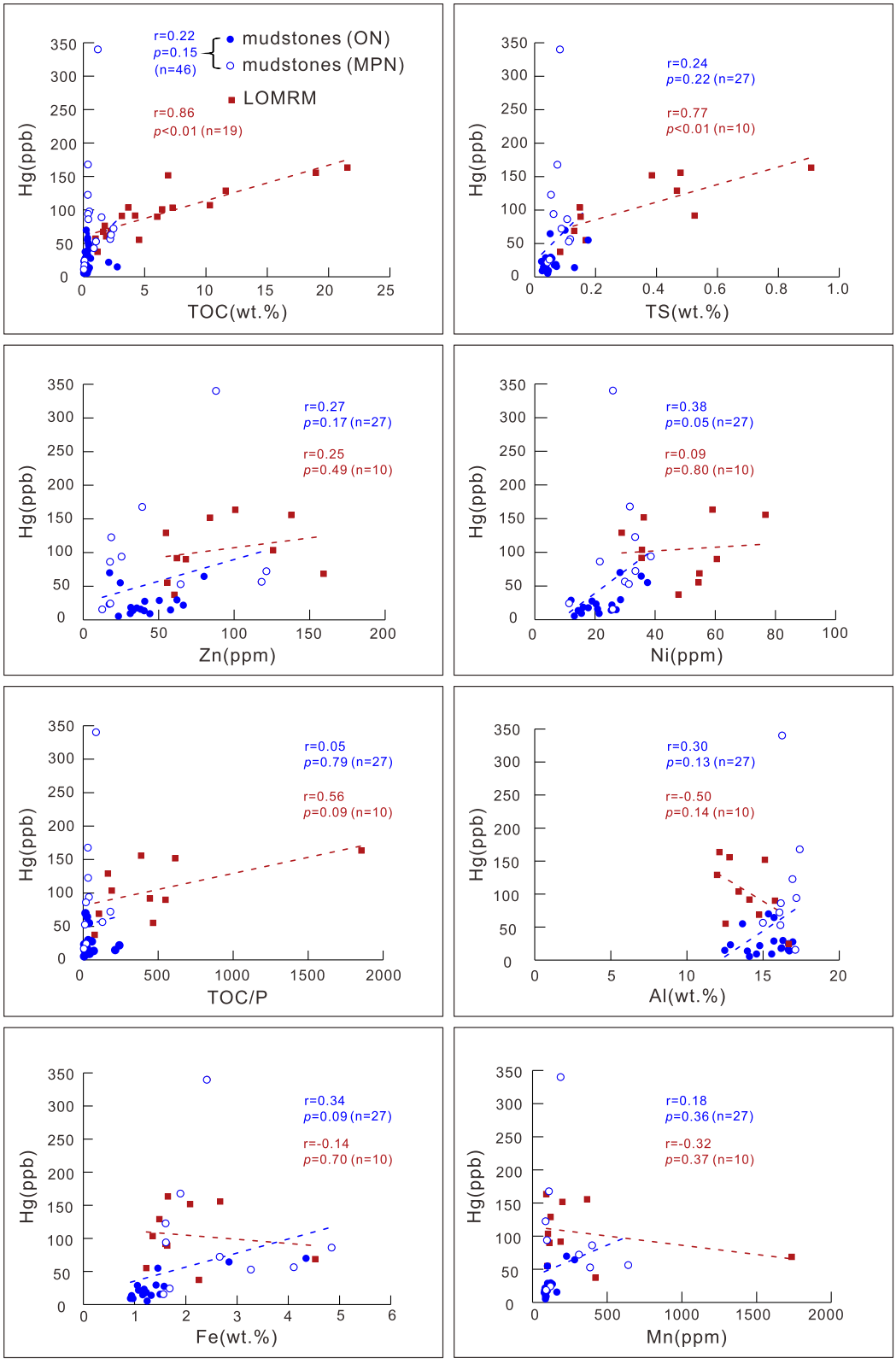

Fig. 3. The relationships of Hg concentrations (ppb) and TOC, element contents and TOC/P ratio (molar) in the mudstones and LOMRM in the Anya section. MPN = main phase of the NCIE. ON = outside the NCIE. LOMRM = laminated organic matter rich mudstones.

tive abundance is coeval with a marked decrease (from 10–20% down to 0–5%) in the relative abundance of all other sporomorphs, including spores, bisaccate pollen of seed fern origin, cycadalean-bennettitalean pollen, and pollen of the Araucariaceae-Cupressaceae (Fig. 5). During the recovery phase of the T-OAE NCIE (~16.1–24.4 m), the palynological assemblages are more diverse, with lower *Classopollis* ratios (20–30% of the palynofacies; Figs. 2 and 5), and with the reappearance of other gymnosperm pollen (5–10%), and spores accounting for ~15% of the sedimentary organic particles (Fig. 5).

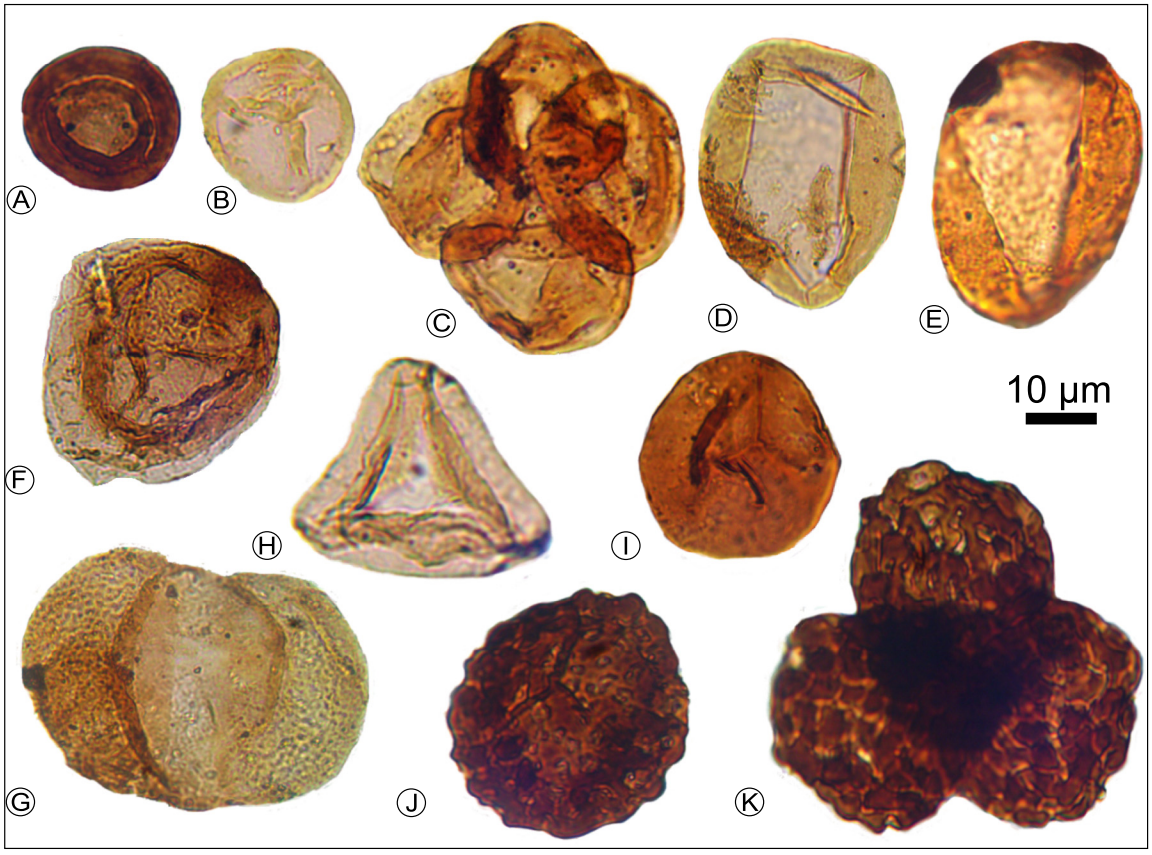

Fig. 4. Representatives of the main palynomorph groups identified during the palynofacies analysis from the Anya section. The scale bar is 10 µm and refers to each micrograph. A. *Classopollis* sp. single grain, 21.6 m. B. *Classopollis qiyangensis* Shang, 1981 single grain, 20.6 m. C. *Classopollis* sp. tetrad, 16.7 m. D. Bennettitalean pollen, *Chasmatosporites apertus* Nilsson, 1958, 20.6 m. E. Bennettitalean pollen, *Chasmatosporites hians* Nilsson, 1958, 5.8 m. F. Cupressaceae-related pollen grain *Perinopollenites elatoides* Couper, 1958, 13.7 m. G. Bisaccate pollen grain of the seed ferns, *Alisporites* sp., 22.2 m. H. Fern spore *Dictyophyllidites harrisii* Couper, 1958, 21.6 m. I. Fern spore *Todisporites minor* Couper, 1958, 16.7 m. J. Schizaceae fern spore *Ischyosporites variegatus* (Couper, 1958) Schulz, 1967, 22.2 m. K. Lycopsid spore tetrad *Leptolepidites* sp., 16.7 m.

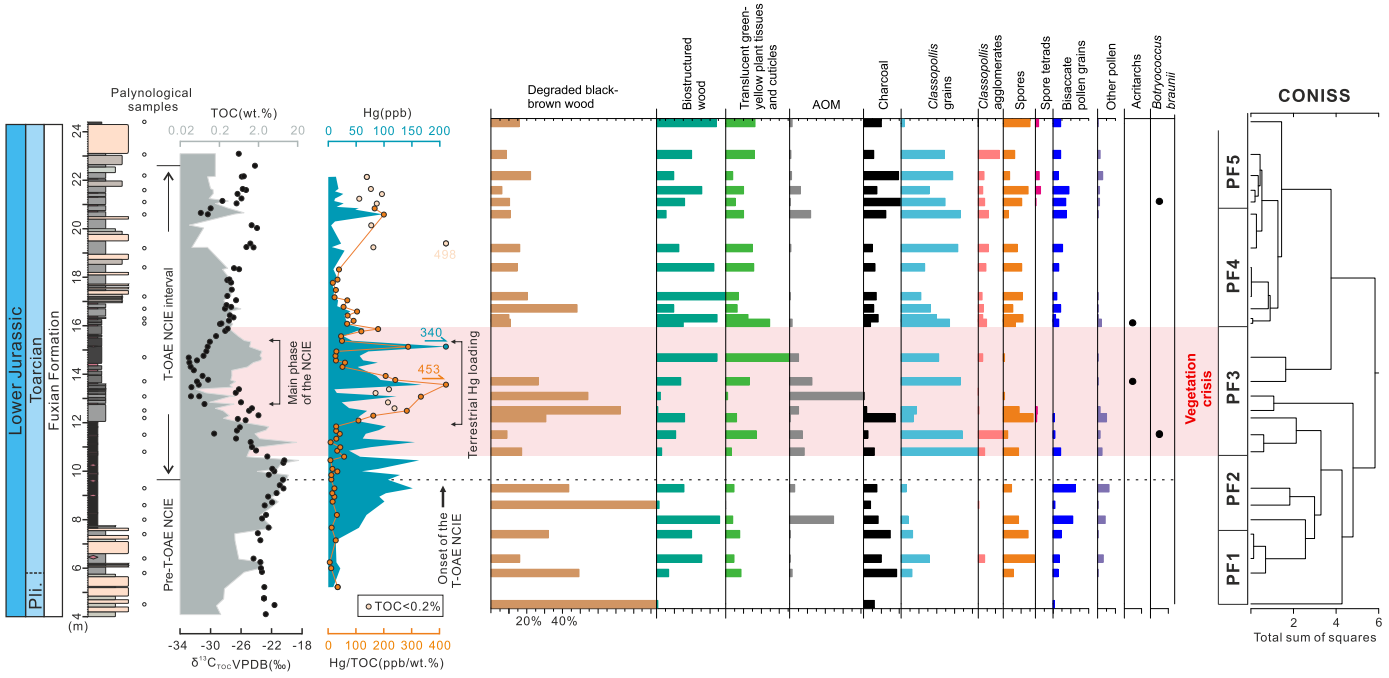

Fig. 5. Palynofacies trends in the Anya section during the T-OAE. AOM = Amorphous organic matter. The group "Other pollen grains" includes cycadalean-bennettitalean pollen, Araucariaceae and Cupressaceae-related pollen. Palynofacies trends are defined as percentage proportion based on counting at least 300 sedimentary organic particles. Local informal palynomorph assemblages (PF 1–5) are determined by stratigraphically constrained cluster analysis (CONISS, Grimm, 1987).

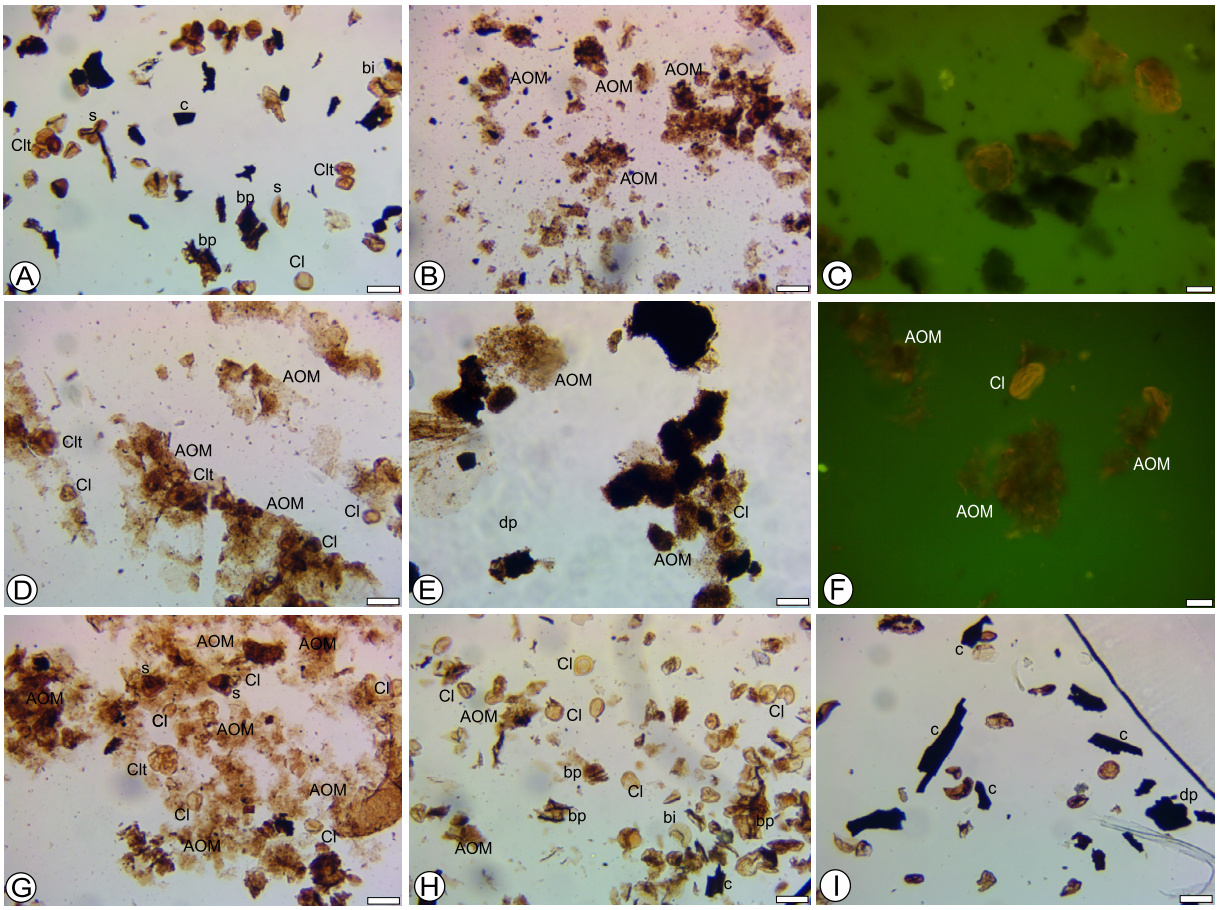

Fig. 6. Selected palynofacies types and kerogen particles from the Anya section. The scale bar is 50 μm, except in C and F where it is 20 μm. Abbreviation of the various organic particles: AOM = amorphous organic matter, bi = bisaccate pollen grain, bp = biostructured phytoclasts (includes biostructured wood and translucent green-yellow plant tissues), c = charcoal, Cl = *Classopollis* grains, Clt = *Classopollis* tetrads and other agglomerates, dp = degraded black-brown wood, s = spores. A. Palynofacies 1 at 6.4 m. Note the predominance of various phytoclast types and spores and pollen grains. B. Palynofacies 2 at 8.0 m from the black shales. Note the predominance of AOM. C. Palynofacies 2 at 9.3 m in fluorescence mode, under incident blue light. Note the weak/lack of autofluorescence of AOM particles that is markedly different from the clotted appearance of AOM in F. D. Palynofacies 3 at 11.5 m showing the predominance of AOM and *Classopollis* grains. E. Palynofacies 3 at 13.1 m. Note the predominance of AOM and degraded black-brown wood particles. F. Palynofacies 3 at 14.7 m in florescence light, under incident blue light. Note the weak autofluorescence and "clotted" appearance of the AOM. G. Palynofacies 3 at 14.7 m. Note the predominance of AOM and *Classopollis* grains. H. Palynofacies 4 at 20.6 m. Note the predominance of *Classopollis* grains and heterogeneity of kerogen particles with the mixture of AOM, biostructured phytoclasts and charcoal particles. I. Palynofacies 5 at 21.6 m. Note the predominance of charcoal and elongated lath-shaped biostructured phytoclasts.

5. Discussion

5.1. Hg source

To interpret the Hg signal, it is important to first identify the main Hg host in the studied sediments. Organic matter, sulfide (i.e. pyrite), and clay minerals are generally thought to be the main host phases of Hg in ancient sediments (Grasby et al., 2019; Shen et al., 2019; Jin et al., 2022). Fe-Mn oxyhydroxides may also play an effective role in the sequestration of Hg in some cases (Yao et al., 2021). Redox variations can also influence the Hg abundance in sediments (e.g., Shen et al., 2020). Changes in depositional environment could be accompanied by a change of Hg host (Them et al., 2019).

In the Anya section, most Hg samples of LOMRM and mudstones (ca. 7.7–17 m) are from deep-lake facies (Jin et al., 2020), suggesting that the Hg accumulation is independent of changes in facies. The high Hg concentrations in the LOMRM interval can be generally attributed to high TOC content (avg. = 6.1 wt.%), this unit showing strong positive correlations between Hg and TOC ($r = 0.86$; Fig. 3). Hg and TOC show a negligible correlation in the mudstones, where TOC content (avg. = 0.6 wt.%) are much lower than in the LOMRM (avg. = 6.1 wt.%), suggesting that the small TOC fluctuations in the mudstones did not control changes in Hg abundance.

In LOMRM, there is a positive correlation between Hg and TS ($r = 0.77$) with average total sulfur (TS) concentrations of 0.34 wt.%. TS concentrations in mudstone are on average 0.07 wt.%, and are not correlated with Hg concentrations (see also SD). It has been shown that sulfides can be the main host of Hg in sediments formed under strong euxinic conditions, with TS values above 1% (Shen et al., 2020). Hence, we can exclude that at Anya sulfides are the dominant Hg-hosts, both in the LOMRM and mudstones. This is further supported by sulfide-host elements (e.g., Zn and Ni), which both have weak/negligible correlations with Hg (Fig. 3). The TOC/P ratio (molar) is a proxy for redox conditions (e.g., Algeo and Ingall, 2007). In the Anya section, a moderately positive correlation was found between TOC/P ratio and Hg in the LOMRM ($r = 0.56$, $p = 0.09$; Fig. 3). The significance of the correlation may be limited by the low number of data, but suggests that local redox changes may have still partially influenced Hg accumulation in some levels of the LOMRM. No correlation ($r = 0.05$, $p = 0.79$) was found between TOC/P ratio and Hg in the mudstones.

Consistently weak/negligible and insignificant correlations exist between Hg concentrations and Fe, Mn and Al in mudstones (Fig. 3). This suggests that iron oxides and clay minerals were not

the main sinks on Hg concentrations in mudstones of the studied section. It is worth noting that the pyritization of the wood fragments may have also influenced the Hg record (Fantasia et al., 2019). However, low TS concentrations (avg. = 0.07 wt.%) and TOC content (avg. = 0.6 wt.%) in mudstones imply a low pyrite content. The negligible correlations between TS and TOC with Hg indicate that post-depositional Hg remobilization and fixing by pyrite cannot account for the Hg anomalies in the mudstones.

In summary, a variety of factors may have influenced Hg accumulation in the studied rocks, though OM appears to be the major host phase for Hg, hence normalization of Hg concentrations with TOC (>0.2 wt.%). Sulfides could potentially be an additional Hg host in the LOMRM, but their contribution could be limited as shown by low TS concentrations. In the mudstones, low TS concentrations and no correlation between TOC/P ratio and Hg, exclude that sulfides are the dominant Hg host; similarly, Hg concentrations are not correlated with elements that are associated with iron oxides and clay minerals, indicating that Hg is not mainly stored in these phases; hence, we can conclude that the main host of Hg in the mudstones must be still OM, as is the case in most of modern and ancient environmental conditions (Grasby et al., 2019; Shen et al., 2020).

Hg-MIF originates from aqueous photoreduction of Hg^{2+} to $Hg^0_{(gas)}$, leaving waters (including cloud vapor) with positive Δ^{199}Hg values, resulting in positive Δ^{199}Hg values in sediments dominated by atmospheric Hg^{2+} deposition. In contrast, soil and vegetation normally tend to have negative Δ^{199}Hg values because they preferentially capture $Hg^0_{(gas)}$. When plants take up Hg, further MDF and MIF occurs, resulting in more negative δ^{202}Hg and Δ^{199}Hg vegetation signatures (Bergquist and Blum, 2007). The Hg emitted via volcanic and hydrothermal activity yields near-zero MIF values (Yin et al., 2016). Taken together, Hg-data from the Anya section is consistent with a dominant terrestrial Hg source into the lake system, showing values similar to modern terrestrial soils and plants (Yin et al., 2016), and modern lake sediments (Chen et al., 2016). Overall, all Δ^{199}Hg and δ^{202}Hg values are <0‰, which is consistent with negative foliage δ^{202}Hg values ranging from −2‰ to −4‰ (Blum et al., 2014) and inconsistent with a volcanic origin. Equally, even if some of the Hg in the section was of volcanic origin, this contribution was likely to have been minor given the broadly invariant Hg-isotope signatures, which is inconsistent with the large-scale changes in volcanic activity over the studied time interval (Moulin et al., 2017). Terrestrial Hg loading has also been documented in a shallow-water marine environment during the T-OAE interval (Them et al., 2019). The notion that the Hg-isotope profile at Anya has a strong terrestrial signal resonates well with observations of modern-day mercury cycling, which indicates that the main natural sources of Hg on the continents are terrestrial biomass and geogenic or legacy Hg emissions from soils and vegetation (Zhou et al., 2021).

5.2. Vegetation crisis in the Ordos Basin

Our data indicate that higher terrestrial Hg loading at the Anya section is coincident with an interval of floral crisis within the T-OAE NCIE (Fig. 5), suggesting a link between significant terrestrial biomass loss and Hg enrichment in the Ordos lake. High relative *Classopollis* abundances occur in many lower Toarcian successions from the Northern Hemisphere across a wide latitudinal and longitudinal gradient (Zakharov et al., 2006; Pieńkowski et al., 2016; Correia et al., 2018; Fonseca et al., 2018; Kemp et al., 2019; Slater et al., 2019). On the North China block, increased *Classopollis* ratios are recorded from inland areas (see summary in Zhang et al., 2022); from Inner Mongolia, Junggar Basin, Qaidam Basin (Wang et al., 2005), Sichuan Basin (Xu et al., 2017) and the Ordos Basin (Jin et al., 2020). This simultaneous and supra-regional increase in *Classopollis* during the T-OAE was likely linked to climatic warming and/or stressed habitats. *Classopollis* was produced by the extinct Cheirolepidiaceae conifers that are generally considered as thermophilic, drought-resistant plants (Vakhrameev, 1991) that could have inhabited upland and lowland environments as well with probably large interspecific ecological flexibility (de Araujo Carvalho et al., 2017). *Classopollis* pollen is often predominant in lagoons and marine nearshore environments, and is often associated with evaporites (e.g., Vakhrameev, 1991). Indeed, Cheirolepidiaceae conifers possessed some physiological traits with xeromorphic epidermal features in particular that can provide adaptive advantages in periods of (but not exclusively) water shortage (Haworth and McElwain, 2008). Other features include enhanced water repellence during extreme rainfall, as well as protection from excess light, pathogens, and atmospheric aerosols (Haworth and McElwain, 2008). Global warming accompanied by enhanced seasonality, erratic precipitation patterns together with volcanogenic particles or other aerosols in the atmosphere could have been present during the T-OAE and explain the proliferation of Cheirolepidiaceae during the early Toarcian (Slater et al., 2019).

In the North China block there is compelling palaeobotanical and palynological evidence for a shift to warmer and/or at least seasonally drier climatic conditions during the early Toarcian (Wang et al., 2005; Zhang et al., 2022). Adjacent to the Ordos Basin to west in the Qaidam Basin, subtropical ferns Dipteridaceae, Matoniaceae, Marattiaceae, and Schizaceae increased in abundance during the early Toarcian, suggesting rising temperatures leading to the expansion of subtropical tropical vegetation belts to the north (Wang et al., 2005; Zhang et al., 2022). Simultaneously, coal formation ceased in the North China block during the early Toarcian indicating, locally at least, seasonally arid conditions that contrast with the widespread distribution of Pliensbachian and Aalenian-Bajocian coal seams (Wang et al., 2005). This scenario concurs with an early Toarcian regional semiarid climate inferred from the presence of redbeds, calcretes, dolomites and gypsum in the paleosol profile from the Sichuan Basin, which was adjacent to the Ordos Basin studied here (Li et al., 2020).

The members of Cheirolepidiaceae were likely better adapted to these climatic and environmental upheavals, as compared to spore-producing plants and other gymnosperms. The decrease of spores and gymnosperm pollen (*Classopollis* excluded) in the Anya section (Fig. 5) indicates that in the studied area seed ferns and spore-producing plants representing lowland and riparian vegetation suffered major losses, as observed in other terrestrial successions during the T-OAE (Pieńkowski et al., 2016; Slater et al., 2019). Moreover, the spores and pollen types that disappeared (Fig. 5) were produced by plants inhabiting mid-canopy and understory vegetation, indicating a collapse of the vegetation structure and deforestation (Slater et al., 2019). The vegetation turnover consequently led to changes in the landscape with denudated lowlands and enhanced soil erosion that facilitated the transport and wash-in of terrestrially-sourced Hg into the Ordos lake basin.

5.3. Terrestrial Hg cycling and its environmental implications

Our data highlight how increased Hg loading in the lake sediments during the T-OAE was not exclusively related to elevated volcanic Hg from Karoo-Ferrar LIP, as suggested by Percival et al. (2015) in studies of marine successions, but rather to a vegetation crisis that changed the erosional and runoff regime of the hinterland. The Ordos lake experienced a significant terrestrial influx during the NCIE interval, as inferred from the increase in non-destructed biostructured wood particles and translucent green-yellow plant tissues in the palynofacies (Fig. 5), suggesting a more vigorous hydrological cycle (Kemp et al., 2019; Rodrigues et al., 2021). However, the precipitation was likely very seasonal as

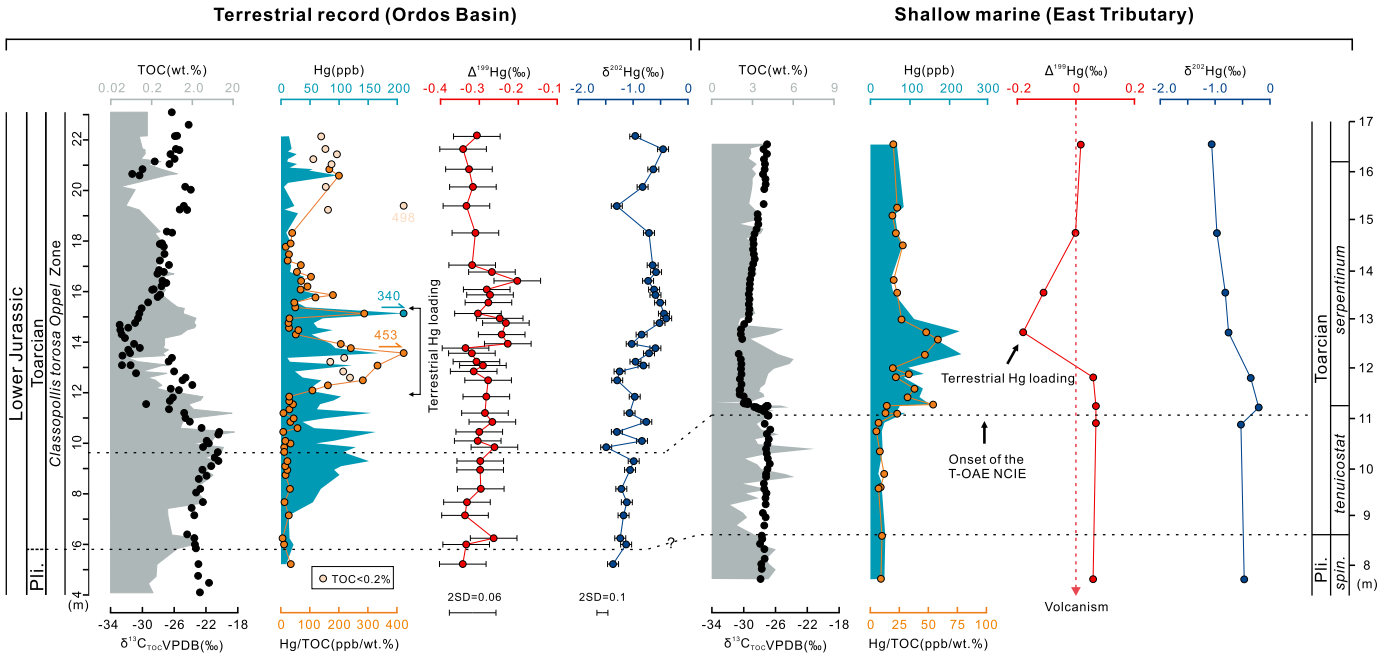

Fig. 7. Comparison of terrestrial and shallow marine Hg-isotope records. Both records support the inference of terrestrial Hg loading during the most negative $\delta^{13}C_{TOC}$ values of the T-OAE. East Tributary data are from (Them et al., 2019).

the high abundance of opaque phytoclasts is favored by seasonal climates and/or with water table fluctuations (e.g., Tyson, 1995; Rodrigues et al., 2021), and that could be the case for the NCIE interval at Anya as well.

Fossil charcoal data is often linked to paleo-wildfire activity (e.g., Baker, 2022). The charcoal data from Anya show similarities to the published charcoal curves from the Western Tethys realm from Peniche (Portugal) and the Mochras Farm (Llandbedr) borehole (Baker et al., 2017), which also record a brief rise in charcoal abundance at the onset of the T-OAE (10.8–12.5 m in Anya) and a subsequent decline during the main phase of the NCIE interval (as seen between 12.8 and 15.4 m in Anya). This trend was linked to an increase in wildfire-activity during the T-OAE initiation at both European sites (Hesselbo et al., 2000; Baker et al., 2017). Likely, climatic and vegetation changes starting in the late Pliensbachian and occurring over a few hundred to thousand years close to the onset of the T-OAE culminated in the rise in fire activity (Hesselbo et al., 2000; Baker et al., 2017). At Anya, we also record a second phase of possibly increased fire activity coincident with the second negative carbon isotope excursion at 20–22 m. This interval might be the precursor of enhanced wildfires in the aftermath of the T-OAE, which was linked to rising pO_2 due enhanced organic carbon burial (Baker et al., 2017; Baker, 2022).

As noted above, the increased Hg input (higher Hg/TOC) into Anya Lake was predominantly terrestrial during the whole T-OAE rather than volcanic. During the crisis, Hg was released from terrestrial biomass through wildfires and weathering, and subsequently transported to the depositional environment. Previous work has also suggested enhanced terrestrial Hg loading to proximal (nearshore) marine sections (Them et al., 2019), based on a negative Hg-MIF shift (−0.2‰) coincident with Hg/TOC peaks in a shallow marine section from eastern Panthalassa, albeit defined by just two datapoints (Fig. 7). Hg/TOC anomalies are not always observed in deeper water settings during the T-OAE (Them et al., 2019), even though deeper water facies are thought to be a good archive for volcanically-derived Hg (Them et al., 2019). This may be related to redistribution/recycling of Hg in intermediate reservoirs after its initial release from volcanic activity, and enhanced Hg loading from terrestrial reservoirs that may mask the volcanic Hg signal (Grasby et al., 2017; Them et al., 2019). As such, the pattern of the Hg record in the Anya section does not exclude the possibility that the Hg was initially sourced from volcanic eruption, i.e., Karoo-Ferrar LIP. The first pulse of the Karoo-Ferrar LIP was at the Pliensbachian/Toarcian boundary (Percival et al., 2015), which caused the first major shift in land plant communities (Slater et al., 2019). Protracted LIP activity could have culminated in the early Toarcian causing the observed land ecosystem collapse and a major turnover of marine biota during the NCIE (Slater et al., 2019). Our data indicate that this ecosystem collapse drove a significantly enhanced terrestrial Hg flux to lakes and nearshore marine environments.

Carbon emissions from the high latitude Karoo-Ferrar LIP likely triggered the warming associated with the T-OAE, though recent atmospheric CO_2 reconstructions using $\delta^{13}C$ have also emphasized that a solely volcanic carbon source is incompatible with the observed rise in pCO_2 (Ruebsam et al., 2020). Deep sedimentary reservoirs (e.g., methane hydrate) (Hesselbo et al., 2000; Kemp et al., 2005) and/or surficial reservoirs (e.g., wetlands/permafrost) (Ruebsam et al., 2020) may have also released substantial carbon to the atmosphere, leading to increased global warming (ca. 6–10 °C) (Suan et al., 2008) and helping to drive turnover in terrestrial ecosystems (Slater et al., 2019).

Atmospheric warming also affected global weather systems with enhanced hydrological cycling that would have caused more vigorous monsoon activity and extreme wet and dry seasons where precipitation fell as heavy downpours (Loope et al., 2001). The resultant intense weathering and degradation of organic matter would have triggered increased terrestrial Hg loading delivered by enhanced continental runoff (Baranyi et al., 2016; Kemp et al., 2019). Warming may have further promoted organic matter degradation by enhancing fungal detritivore activity (Pieńkowski et al., 2016). Additionally, high atmospheric pCO_2 levels (McElwain et al., 2005; Ruebsam et al., 2020) likely suppressed plant transpiration, which could also enhance runoff (Gedney et al., 2006).

Enhanced hydrological cycle and floral turnovers characterize other Palaeozoic and Mesozoic major biological crises, such as the Permian–Triassic mass extinction (Algeo et al., 2011) and the End-Triassic mass extinction (Steinthorsdottir et al., 2012). The

Hg anomalies that mark these events could have been therefore also triggered by vegetation changes, enhanced weathering rates and the leaching and subsequent transport of mercury to lacustrine and/or marine depositional settings. Indeed, modeling has shown that massive oxidation of terrestrial biomass could drive major enhancements of Hg loading to marine and terrestrial depositional environments during mass extinctions (Dal Corso et al., 2020). Constraining the source and pathways of mercury by combining concentration and isotopic data is therefore relevant for all volcanically-driven events (e.g., Grasby et al., 2019; Yager et al., 2021; Shen et al., 2022).

The Hg cycle is closely linked to the cycling of organic matter (Meili, 1991), and inputs of terrestrial Hg into the ocean would have also been coupled to inputs of organically-bound nutrients such as N and P. Nutrient delivery driven by enhanced hydrological cycling would have promoted oxygen consumption in the oceans, promoting anoxia, whilst also allowing toxic Hg to enter the food chain. Using previous cyclostratigraphic constraints for the entire NCIE, the delivery of Hg into the ocean may have lasted up to 300–900 kyr (Boulila et al., 2019; Suan et al., 2008). Such protracted delivery of excess terrestrial Hg into the ocean, particularly in proximal environments (Them et al., 2019), may have been an additional driver of marine extinctions (Grasby et al., 2020). Modeling work on the Permian−Triassic extinction event has shown that large-scale Hg release by Siberian Trap eruptions would have been extremely toxic to marine and terrestrial life (Grasby et al., 2020). We suggest that in the case of the T-OAE that release of the terrestrial Hg pool could have been an additional factor in triggering a biotic crisis besides rapid palaeotemperature rise (Suan et al., 2008). Our work highlights how terrestrial ecosystems were strongly affected by climate change during the early Toarcian, and how coupled changes in the Hg cycle can elucidate this. Although primarily known for the expansion of organic-rich facies and deoxygenation in marine settings, our work underlines how the T-OAE was first and foremost a major Phanerozoic hyperthermal that triggered crises in both terrestrial and marine ecosystems. This could have wider implications for in-depth understanding other global mass extinction events related to volcanism.

6. Conclusions

We analyzed sedimentary Hg in an early Toarcian terrestrial sequence of the Ordos Basin (North China). A peak of Hg and Hg/TOC values is observed in mudstones associated with the main NCIE of the T-OAE (Toarcian OAE) and is synchronous with a major vegetation crisis. Hg-isotopes show that terrestrial Hg sources dominated the Anya succession of the Ordos Basin throughout the T-OAE, yielding consistent negative MIF and MDF values, and thus excluding direct increased atmospheric Hg deposition into the lake. Higher terrestrial Hg deposition has been observed also in coeval marine sediments.

Our new terrestrial record allows reconstructing a cascade of events that marked the T-OAE. A major loss of lowland mid-canopy and understory (ferns and seed ferns) led to deforestation and slope destabilization, and enhanced loading of terrestrially-sourced Hg into the Ordos Lake. The recycling of terrestrial Hg is likely linked to the climatic feedbacks of high atmospheric pCO_2 levels resulted from multiple sources such as the injection of ^{12}C-enriched methane and/or volcanic gases. The subsequent global warming drove the acceleration of the hydrological cycle and enhanced runoff synchronously with a land ecosystem crisis. Along with Hg, organically-bound elements like the nutrients N and P were transferred into the ocean, being capable of triggering seawater eutrophication and anoxia, while Hg, after entering the food chain, could have been an additional killing agent in the marine ecosystem. This study highlights the importance of coupling Hg concentrations with isotope data to constrain Hg sources and fluxes. This has particular relevance for the study of extinction events linked to volcanism, where the role of terrestrial Hg loading to marine and lacustrine environments (and the potential negative effects of this on life) is underexplored.

CRediT authorship contribution statement

F.Z., J.D.C, and X.J. conceived the idea and led the study; V.B. performed palynological analysis; D.B.K. and W.H.C. performed Hg concentration analysis; X.B.F. and G.Y.S. performed Hg isotope analysis. X.J. and Z.Q.S. performed field investigation and sampling; J.D.C performed sulfur concentration analysis; F.Z. performed major and trace elements analyses; X.J. and V.B. primarily wrote the manuscript with valuable input from S.E.G, D.B.K, J.D.C, and F.Z. All authors contributed to the discussion and interpretation of the data.

Declaration of competing interest

The authors declare that they have no known competing financial interests or personal relationships that could have appeared to influence the work reported in this paper.

Data availability

Data are provided in the supplementary materials

Acknowledgements

We are grateful to Omid H. Ardakani and Vivi Vajda for their constructive comments that helped to improve the manuscript, and to the Editor Boswell Wing for the handling of our manuscript. We thank the following colleagues for their contribution to our work: F. Wu (SKLLQG, Xi'an); X. Yu (carbon isotope, TOC); H. Song and Y. Du (S concentration, CUG Wuhan). This work was supported by the National Natural Science Foundation of China grants (41902106; 41888101; 42172031); the Youth Innovation Promotion Association of CAS (2020406); the 2nd Tibetan Plateau Scientific Expedition and Research (2019QZKK0707); and State Key Laboratory of Loess and Quaternary Geology (SKLLQGPP2204, SKLLQGZR2005). V. Baranyi was supported by the Croatian Geological Survey through program funding provided by the Croatian Ministry of Science and Education. This is a contribution to the IGCP 739 (The Mesozoic-Palaeogene hyperthermal events).

Appendix A. Supplementary material

Supplementary material related to this article can be found online at https://doi.org/10.1016/j.epsl.2022.117842.

References

Algeo, T.J., Chen, Z.Q., Fraiser, M.L., Twitchett, R.J., 2011. Terrestrial–marine teleconnections in the collapse and rebuilding of Early Triassic marine ecosystems. Palaeogeogr. Palaeoclimatol. Palaeoecol. 308, 1–11.

Algeo, T.J., Ingall, E., 2007. Sedimentary corg: P ratios, paleocean ventilation, and Phanerozoic atmospheric PO_2. Palaeogeogr. Palaeoclimatol. Palaeoecol. 256, 130–155.

Bailey, T., Rosenthal, Y., McArthur, J., Van de Schootbrugge, B., Thirlwall, M., 2003. Paleoceanographic changes of the Late Pliensbachian–Early Toarcian interval: a possible link to the genesis of an Oceanic Anoxic Event. Earth Planet. Sci. Lett. 212, 307–320.

Baker, S.J., 2022. Fossil evidence that increased wildfire activity occurs in tandem with periods of global warming in Earth's past. Earth-Sci. Rev. 224, 103871.

Baker, S.J., Hesselbo, S.P., Lenton, T.M., Duarte, L.V., Belcher, C.M., 2017. Charcoal evidence that rising atmospheric oxygen terminated Early Jurassic ocean anoxia. Nat. Commun. 8, 15018.

Baranyi, V., Pálfy, J., Görög, Á., Riding, J.B., Raucsik, B., 2016. Multiphase response of palynomorphs to the Toarcian oceanic anoxic event (Early Jurassic) in the Réka Valley section, Hungary. Rev. Palaeobot. Palynol. 235, 51–70.
Bergquist, B.A., Blum, J.D., 2007. Mass-dependent and -independent fractionation of Hg isotopes by photoreduction in aquatic systems. Science 318, 417–420.
Blum, J.D., Sherman, L.S., Johnson, M.W., 2014. Mercury isotopes in Earth and environmental sciences. Annu. Rev. Earth Planet. Sci. 42, 249–269.
Boulila, S., Galbrun, B., Sadki, D., Gardin, S., Bartolini, A., 2019. Constraints on the duration of the early Toarcian T-OAE and evidence for carbon-reservoir change from the High Atlas (Morocco). Glob. Planet. Change 175, 113–128.
Caruthers, A.H., Smith, P.L., Gröcke, D.R., 2014. The Pliensbachian–Toarcian (Early Jurassic) extinction: a North American perspective. In: Keller, G., Kerr, A.C. (Eds.), Volcanism, Impacts, and Mass Extinctions: Causes and Effects. In: Special Papers of the Geological Society of America, vol. 505, p. 21.
Chen, J., Hintelmann, H., Zheng, W., Feng, X., Cai, H., Wang, Z., Yuan, S., Wang, Z., 2016. Isotopic evidence for distinct sources of mercury in lake waters and sediments. Chem. Geol. 426, 33–44.
Correia, V.F., Riding, J.B., Duarte, L.V., Fernandes, P., Pereira, Z., 2018. The Early Jurassic palynostratigraphy of the Lusitanian Basin, western Portugal. Geobios 51, 537–557.
Dal Corso, J., Mills, B.J., Chu, D., Newton, R.J., Mather, T.A., Shu, W., Tong, J., Wignall, P.B., 2020. Permo–Triassic boundary carbon and mercury cycling linked to terrestrial ecosystem collapse. Nat. Commun. 11, 1–9.
de Araujo Carvalho, M., Lana, C.C., Bengtson, P., de Paula Sá, N., 2017. Late Aptian (Cretaceous) climate changes in northeastern Brazil: a reconstruction based on indicator species analysis (IndVal). Palaeogeogr. Palaeoclimatol. Palaeoecol. 485, 543–560.
Dera, G., Pucéat, E., Pellenard, P., Neige, P., Delsate, D., Joachimski, M.M., Reisberg, L., Martinez, M., 2009. Water mass exchange and variations in seawater temperature in the NW Tethys during the Early Jurassic: evidence from neodymium and oxygen isotopes of fish teeth and belemnites. Earth Planet. Sci. Lett. 286, 198–207.
Fantasia, A., Adatte, T., Spangenberg, J.E., Font, E., Duarte, L.V., Föllmi, K.B., 2019. Global versus local processes during the Pliensbachian–Toarcian transition at the Peniche GSSP, Portugal: a multi-proxy record. Earth-Sci. Rev. 198, 102932.
Fantasia, A., Föllmi, K.B., Adatte, T., Bernárdez, E., Spangenberg, J.E., Mattioli, E., 2018. The Toarcian oceanic anoxic event in southwestern Gondwana: an example from the Andean basin, northern Chile. J. Geol. Soc. 175, 883–902.
Fonseca, C., Mendonça Filho, J.G., Lézin, C., Duarte, L.V., Fauré, P., 2018. Organic facies variability during the Toarcian Oceanic Anoxic Event record of the Grands Causses and Quercy basins (southern France). Int. J. Coal Geol. 190, 218–235.
Ge, D.K., Yang, Q., Fu, Z.M., Li, Z., Li, B.F., 1989. The trace fossil and depositional environment of Fuxian Formation, Yulin Country, Northern Shaanxi province. Coal Geol. Explor. 3, 1–6 (in Chinese with English abstract).
Gedney, N., Cox, P.M., Betts, R.A., Boucher, O., Huntingford, C., Stott, P.A., 2006. Detection of a direct carbon dioxide effect in continental river runoff records. Nature 439, 835–838.
Grasby, S.E., Liu, X., Yin, R., Ernst, R.E., Chen, Z., 2020. Toxic mercury pulses into late Permian terrestrial and marine environments. Geology 48, 830–833.
Grasby, S.E., Shen, W., Yin, R., Gleason, J.D., Blum, J.D., Lepak, R.F., Hurley, J.P., Beauchamp, B., 2017. Isotopic signatures of mercury contamination in latest Permian oceans. Geology 45, 55–58.
Grasby, S.E., Them Ii, T.R., Chen, Z., Yin, R., Ardakani, O.H., 2019. Mercury as a proxy for volcanic emissions in the geologic record. Earth-Sci. Rev. 196, 102880.
Grimm, E.C., 1987. CONISS: a FORTRAN 77 program for stratigraphically constrained cluster analysis by the method of incremental sum of squares. Comput. Geosci. 13, 13–35.
Haworth, M., McElwain, J., 2008. Hot, dry, wet, cold or toxic? Revisiting the ecological significance of leaf and cuticular micromorphology. Palaeogeogr. Palaeoclimatol. Palaeoecol. 262, 79–90.
Hesselbo, S.P., Gröcke, D.R., Jenkyns, H.C., Bjerrum, C.J., Farrimond, P., Bell, H.S.M., Green, O.R., 2000. Massive dissociation of gas hydrate during a Jurassic oceanic anoxic event. Nature 406, 392–395.
Huang, Q., Liu, Y., Chen, J., Feng, X., Huang, W., Yuan, S., Cai, H., Fu, X., 2015. An improved dual-stage protocol to pre-concentrate mercury from airborne particles for precise isotopic measurement. J. Anal. At. Spectrom. 30, 957–966.
Jenkyns, H., 1988. The early Toarcian (Jurassic) anoxic event-stratigraphic, sedimentary, and geochemical evidence. Am. J. Sci. 288, 101–151.
Jin, X., Ogg, J.G., Lu, S., Shi, Z., Kemp, D.B., Hua, X., Onoue, T., Rigo, M., 2022. Terrestrial record of carbon-isotope shifts across the Norian/Rhaetian boundary: a high-resolution study from northwestern Sichuan Basin, South China. Glob. Planet. Change 210, 103754.
Jin, X., Shi, Z., Baranyi, V., Kemp, D.B., Han, Z., Luo, G., Hu, J., He, F., Chen, L., Preto, N., 2020. The Jenkyns Event (early Toarcian OAE) in the Ordos Basin, North China. Glob. Planet. Change 193, 103273.
Kemp, D.B., Baranyi, V., Izumi, K., Burgess, R.D., 2019. Organic matter variations and links to climate across the early Toarcian oceanic anoxic event (T-OAE) in Toyora area, southwest Japan. Palaeogeogr. Palaeoclimatol. Palaeoecol. 530, 90–102.
Kemp, D.B., Suan, G., Fantasia, A., Jin, S., Chen, W., 2022. Global organic carbon burial during the Toarcian oceanic anoxic event: patterns and controls. Earth-Sci. Rev. 231, 104086.
Kemp, D.B., Coe, A.L., Cohen, A.S., Schwark, L., 2005. Astronomical pacing of methane release in the Early Jurassic period. Nature 437, 396–399.
Li, X., Wang, J., Rasbury, T., Zhou, M., Wei, Z., Zhang, C., 2020. Early Jurassic climate and atmospheric CO_2 concentration in the Sichuan paleobasin, southwestern China. Clim. Past 16, 2055–2074.
Little, C.T.S., Benton, M.J., 1995. Early Jurassic mass extinction: a global long-term event. Geology 23, 495–498.
Loope, D.B., Rowe, C.M., Joeckel, R.M., 2001. Annual monsoon rains recorded by Jurassic dunes. Nature 412, 64–66.
McElwain, J.C., Wade-Murphy, J., Hesselbo, S.P., 2005. Changes in carbon dioxide during an oceanic anoxic event linked to intrusion into Gondwana coals. Nature 435, 479–482.
Meili, M., 1991. The coupling of mercury and organic matter in the biogeochemical cycle—towards a mechanistic model for the boreal forest zone. Water Air Soil Pollut. 56, 333–347.
Meng, Q.R., Wu, G.L., Fan, L.G., Wei, H.H., 2019. Tectonic evolution of early Mesozoic sedimentary basins in the North China block. Earth-Sci. Rev. 190, 416–438.
Moulin, M., Fluteau, F., Courtillot, V., Marsh, J., Delpech, G., Quidelleur, X., Gérard, M., 2017. Eruptive history of the Karoo lava flows and their impact on early Jurassic environmental change. J. Geophys. Res., Solid Earth 122, 738–772.
Percival, L.M.E., Witt, M.L.I., Mather, T.A., Hermoso, M., Jenkyns, H.C., Hesselbo, S.P., Al-Suwaidi, A.H., Storm, M.S., Xu, W., Ruhl, M., 2015. Globally enhanced mercury deposition during the end-Pliensbachian extinction and Toarcian OAE: a link to the Karoo–Ferrar Large Igneous Province. Earth Planet. Sci. Lett. 428, 267–280.
Pieńkowski, G., Hodbod, M., Ullmann, C.V., 2016. Fungal decomposition of terrestrial organic matter accelerated Early Jurassic climate warming. Sci. Rep. 6, 1–11.
Pyle, D.M., Mather, T.A., 2003. The importance of volcanic emissions for the global atmospheric mercury cycle. Atmos. Environ. 37, 5115–5124.
Rodrigues, B., Silva, R.L., Mendonça Filho, J.G., Reolid, M., Sadki, D., Comas-Rengifo, M.J., Goy, A., Duarte, L.V., 2021. The phytoclast group as a tracer of palaeoenvironmental changes in the Early Toarcian. Geol. Soc. (Lond.) Spec. Publ. 514, 291–307.
Ruebsam, W., Reolid, M., Schwark, L., 2020. $\delta^{13}C$ of terrestrial vegetation records Toarcian CO_2 and climate gradients. Sci. Rep. 10, 1–8.
Selin, N.E., 2009. Global biogeochemical cycling of mercury: a review. Annu. Rev. Environ. Resour. 34, 43–63.
Shen, J., Algeo, T.J., Planavsky, N.J., Yu, J.X., Feng, Q.L., Song, H.J., Song, H.Y., Rowe, H., Zhou, L., Chen, J.B., 2019. Mercury enrichments provide evidence of Early Triassic volcanism following the end-Permian mass extinction. Earth-Sci. Rev. 195, 191–212.
Shen, J., Feng, Q., Algeo, T.J., Liu, J., Zhou, C., Wei, W., Liu, J., Them Ii, T.R., Gill, B.C., Chen, J., 2020. Sedimentary host phases of mercury (Hg) and implications for use of Hg as a volcanic proxy. Earth Planet. Sci. Lett. 543, 116333.
Shen, J., Yin, R., Algeo, T.J., Svensen, H.H., Schoepfer, S.D., 2022. Mercury evidence for combustion of organic-rich sediments during the end-Triassic crisis. Nat. Commun. 13, 1–8.
Slater, S.M., Twitchett, R.J., Danise, S., Vajda, V., 2019. Substantial vegetation response to Early Jurassic global warming with impacts on oceanic anoxia. Nat. Geosci. 12, 462–467.
Steinthorsdottir, M., Woodward, I., Surlyk, F., McElwain, J.C., 2012. Deep-time evidence of a link between elevated CO_2 concentrations and perturbations in the hydrological cycle via drop in plant transpiration. Geology 40, 815–818.
Suan, G., Mattioli, E., Pittet, B., Mailliot, S., Lécuyer, C., 2008. Evidence for major environmental perturbation prior to and during the Toarcian (Early Jurassic) oceanic anoxic event from the Lusitanian Basin, Portugal. Paleoceanography 23, PA1202.
Sun, G., Sommar, J., Feng, X., Lin, C., Ge, M., Wang, W., Yin, R., Fu, X., Shang, L., 2016. Mass-dependent and-independent fractionation of mercury isotope during gas-phase oxidation of elemental mercury vapor by atomic Cl and Br. Environ. Sci. Technol. 50, 9232–9241.
Them, T.R., Jagoe, C.H., Caruthers, A.H., Gill, B.C., Grasby, S.E., Gröcke, D.R., Yin, R., Owens, J.D., 2019. Terrestrial sources as the primary delivery mechanism of mercury to the oceans across the Toarcian Oceanic Anoxic Event (Early Jurassic). Earth Planet. Sci. Lett. 507, 62–72.
Tyson, R.V., 1995. Sedimentary Organic Matter: Organic Facies and Palynofacies. Kluwer Academic, Dordrecht, Holland. 615 p.
Vakhrameev, V.A., 1991. Jurassic and Cretaceous Floras and Climates of the Earth. Cambridge University Press.
Wang, Y., Mosbrugger, V., Zhang, H., 2005. Early to Middle Jurassic vegetation and climatic events in the Qaidam Basin, Northwest China. Palaeogeogr. Palaeoclimatol. Palaeoecol. 224, 200–216.
Xu, W., Ruhl, M., Jenkyns, Hugh C., Hesselbo, Stephen P., Riding, James B., Selby, D., Naafs, B. David A., Weijers, Johan W.H., Pancost, Richard D., Tegelaar, Erik W., Idiz, Erdem F., 2017. Carbon sequestration in an expanded lake system during the Toarcian oceanic anoxic event. Nat. Geosci. 10, 129–134.
Xu, W., Ruhl, M., Jenkyns, H.C., Leng, M.J., Huggett, J.M., Minisini, D., Ullmann, C.V., Riding, J.B., Weijers, J.W.H., Storm, M.S., Percival, L.M.E., Tosca, N.J., Idiz, E.F., Tegelaar, E.W., Hesselbo, S.P., 2018. Evolution of the Toarcian (Early Jurassic) carbon-cycle and global climatic controls on local sedimentary processes (Cardigan Bay Basin, UK). Earth Planet. Sci. Lett. 484, 396–411.
Yager, J.A., West, A.J., Thibodeau, A.M., Corsetti, F.A., Rigo, M., Berelson, W.M., Bottjer, D.J., Greene, S.E., Ibarra, Y., Jadoul, F., Ritterbush, K.A., Rollins, N., Rosas,

S., Stefano, P.D., Sulca, D., Todaro, S., Wynn, P., Zimmermann, L., Bergquist, B.A., 2021. Mercury contents and isotope ratios from diverse depositional environments across the Triassic–Jurassic boundary: towards a more robust mercury proxy for large igneous province magmatism. Earth-Sci. Rev. 223, 103775.

Yao, H., Chen, X., Yin, R., Grasby, S.E., Weissert, H., Gu, X., Wang, C., 2021. Mercury evidence of intense volcanism preceded oceanic anoxic event 1d. Geophys. Res. Lett. 48, e2020GL091508.

Yin, R., Feng, X., Hurley, J.P., Krabbenhoft, D.P., Lepak, R.F., Hu, R., Zhang, Q., Li, Z., Bi, X., 2016. Mercury isotopes as proxies to identify sources and environmental impacts of mercury in sphalerites. Sci. Rep. 6, 1–8.

Yin, R., Feng, X., Shi, W., 2010. Application of the stable-isotope system to the study of sources and fate of Hg in the environment: a review. Appl. Geochem. 25, 1467–1477.

Zakharov, V., Shurygin, B., Il'ina, V., Nikitenko, B., 2006. Pliensbachian-Toarcian biotic turnover in north Siberia and the Arctic region. Stratigr. Geol. Correl. 14, 399–417.

Zhang, M., Ji, L., Wu, Y., He, C., 2015. Palynofacies and geochemical analysis of the Triassic Yanchang formation, Ordos Basin: implications for hydrocarbon generation potential and the paleoenvironment of continental source rocks. Int. J. Coal Geol. 152, 159–176.

Zhang, Q., Gong, E., Zhang, Y., Guan, C., 2022. Palynoflora and palaeoclimate of the late Early Jurassic (Toarcian) in eastern Liaoning, China. Palaeobiodivers. Palaeoenviron. 102, 73–88.

Zhou, J., Obrsit, D., Dastoor, A., Jiskra, M., Ryjkov, A., 2021. Vegetation uptake of mercury and impacts on global cycling. Nat. Rev. Earth Environ. 2, 269–284.